

Pressure-tuning of the electron-phonon coupling: the insulator to metal transition in manganites.

P. Postorino, A. Congeduti, P. Dore, F.A. Gorelli,
L. Ulivi, A. Sacchetti, A. Kumar, D.D. Sarma

October 29, 2018

Abstract

A comprehensive understanding of the physical origin of the unique magnetic and transport properties of $A_{1-x}A'_x\text{MnO}_3$ manganites (A = trivalent rare-earth and A' = divalent alkali-earth metal) is still far from being achieved [1, 2, 3]. The complexity of these systems arises from the interplay among several competing interactions of comparable strength. Recently the electron-phonon coupling, triggered by a Jahn-Teller distortion of the MnO_6 octahedra, has been recognised to play an essential role in the insulator to metal transition and in the closely related colossal magneto-resistance [3]. The pressure tuning of the octahedral distortion gives a unique possibility to separate the basic interactions and, at least in principle, to follow the progressive transformation of a manganite from an intermediate towards a weak electron-phonon coupling regime. Using a diamond anvil cell, temperature and pressure-dependent infrared absorption spectra of $\text{La}_{0.75}\text{Ca}_{0.25}\text{MnO}_3$ have been collected and, from the spectral weight analysis [4], the pressure dependence of the insulator to metal transition temperature T_{IM} has been determined for the first time up to 11.2 GPa. The $T_{IM}(P)$ curve we proposed to model the present data revealed a universality character in accounting for the whole class of intermediate coupling compounds. This property can be exploited to distinguish the intermediate from the weak coupling compounds pointing out the fundamental differences between the two coupling regimes.

The crystal structure of manganites consists of a pseudocubic lattice of MnO_6 octahedra with the $A-A'$ ions placed in the free volume among them. In doped compounds ($0 < x < 1$), the Mn ions assume the $\text{Mn}^{+3}/\text{Mn}^{+4}$ mixed-valence and the Mn^{+3}O_6 octahedra undergo an asymmetric distortion which removes the degeneracy of the outer Mn d-orbital with e_g symmetry (Jahn-Teller (JT) effect). The presence of distorted octahedra in the pseudocubic lattice gives rise to a local potential well which, in turn, tends to localise the e_g -electrons. This self-trapping mechanism is a fingerprint of the electron-phonon coupling (EPC) whose strength depends on the extent of JT distortion. Therefore, tuning the asymmetry of the Mn^{+3}O_6 by means of the so-called *internal pressure* (chemical substitution which changes

the average $A - A'$ ionic radius R_A) [5, 6, 7] or by an external pressure (hydrostatic pressure P) [8, 9, 10, 11, 12, 13, 14, 15, 16, 17], is an intriguing way to probe the EPC and its localising tendency.

EPC profoundly affects the transport properties of manganites, which range from insulating (strong EPC) to metallic (weak EPC) character [18]. At intermediate-coupling (IC), several manganites ($0.2 < x < 0.5$) show Colossal Magneto-Resistance (CMR) and, on cooling, they undergo a first-order insulator-to-metal (IM) transition, whereas Weak-Coupling (WC) systems show moderate magneto resistance and a continuous IM transition [18, 19, 20]. Since the temperature T_{IM} is expected to be proportional to the effective e_g orbital bandwidth W_{eff} [6, 8], shifts in T_{IM} can be produced by forcing W_{eff} to change. This can be achieved by a pressure-tuning of the EPC, which behaves as a narrowing factor $\xi \leq 1$ applied on the bare structural term W_0 [7], that is $T_{IM} \propto W_{eff} = W_0 \xi$ [8, 21]. *Internal* or external applied pressure cause an increase of T_{IM} through the double mechanism of enlarging W_0 by enhancement of the Mn-O bond covalency, and of increasing ξ by a reduction of the EPC strength. Exploiting chemical substitution, R_A - T phase diagrams have been obtained [5, 22], whereas a set of $T_{IM}(P)$ data [8, 9, 10, 11, 12, 13, 14, 15, 16, 17] is available up to a maximum of 2 GPa, owing to the many difficulties of high-pressure transport and magnetic measurements. The experimental data suggest an equivalence between *internal* and external pressure [5]: the same change of T_{IM} can be achieved by varying either the average ionic radius by ΔR_A or the pressure by $\Delta P = \Delta R_A / \beta$ ($\beta = 3.7 \cdot 10^{-3}$ Å/GPa [5]). Nevertheless, external pressure has the clear advantage of operating on a single sample in a continuous way and under conditions more controlled than chemical substitution.

The IM transition can be conveniently described in terms of polarons, quasi-particles associated to a charge plus the surrounding lattice distortion. Indeed, a picture of localized polarons is associated to the paramagnetic-insulating phase of the manganites, whereas in the ferromagnetic-metallic phase below T_{IM} , the increase of the e_g -electron kinetic energy, due to the magnetic double-exchange interaction, favors polarons itinerancy [4, 23, 24]. Since the transition of polarons from localised states to the continuum gives rise to a large band centred in the near Infrared (IR)[4, 24] the delocalization process can be monitored by spectroscopic techniques. Indeed, the band-profile reflects the distribution of the polaron binding energies and the spectral weight, that is the frequency-integrated absorption spectrum, provides a measure of the e_g -electron kinetic energy and, hence, of the polaron mobility [4, 24, 25]. Exploiting the

advantage of coupling of Diamond Anvil Cells (DAC) to IR spectroscopy [4], the delocalization process can be monitored over an extended and, until now, unexplored pressure region.

$\text{La}_{0.75}\text{Ca}_{0.25}\text{MnO}_3$ ($T_{IM}(P=0)=220$ K [4]) was chosen as a suitable IC candidate for the present experiment and temperature-dependent IR spectra (100-320 K) were collected along several isobaric paths ($0 < P < 11.2$ GPa) over the 500-4500 cm^{-1} spectral range. The DAC equipped with 600 μm culet IIA diamonds and steel gasket (300- μm diameter and 50- μm deep hole) was mounted on the cold finger of a cryocooler. The Bruker 120HR interferometer, at LENS (European Laboratory for Non-Linear Spectroscopy, Florence), was equipped with a KBr beam-splitter and an MCT detector. High-quality measurements, in spite of the high absorbance and the small size of the sample, were obtained thanks to the high-efficiency focusing system [26]. The sample, prepared by a solid state reaction method [27], was finely milled and smeared on the top surface of a KBr pellet sintered inside the gasket hole [4]. The optical density $Od(\nu) = \ln[I_0(\nu)/I(\nu)]$ was obtained by measuring the intensities $I_0(\nu)$ and $I(\nu)$, transmitted by the pure KBr pellet and by the KBr plus sample [4]. The $Od(\nu)$ measured along three representative isobaric paths at selected temperatures are shown in Fig. 1. The intense peak around 600 cm^{-1} is due to the IR active B_{2u} phonon mode [4], while the broader structures around 1000 cm^{-1} and 1400 cm^{-1} originate from multi-phonon processes, enhanced by resonance effects [28]. The phonon nature of these features is confirmed by their moderate pressure-induced frequency hardening [4, 29]. The phonon spectrum is superimposed to a broad and intense contribution, which extends over the whole spectral range, is strongly temperature and pressure dependent and arises from the low frequency side of the polaronic band. Upon cooling at a given pressure, the overall absorption decreases (red spectra) until an *inversion temperature* is reached, where the trend is reversed and the absorption starts to increase (blue spectra). The *inversion temperature* identifies T_{IM} [4], since the observed absorption trend corresponds to what expected for the mobility of the charge carriers in the insulating or metallic phase. The temperature dependence of the spectral weights $n^*(T)$ at different pressures was obtained by integrating the measured $Od(\nu)$ over the 800-1800 cm^{-1} range. In Fig. 2 $n^*(T)$ are shown by red and blue symbols to distinguish the insulating ($dn^*/dT < 0$) from the metallic ($dn^*/dT > 0$) regime [4, 18]. Fig. 2 shows that at fixed temperature $dn^*/dP > 0$, meaning that pressure causes an increase of polaron mobility over the whole temperature range. At low-temperatures ($T < 150\text{K}$), all the $n^*(T)$ seem to con-

verge towards the same asymptotic curve, suggesting the occurrence of a sort of *asymptotic metal* state, consistent with the picture of fully itinerant polarons.

The fine temperature sampling of $n^*(T)$ enables an accurate determination of the $T_{IM}(P)$ values, shown in the P-T phase diagram of Fig. 3a. The deviation from linearity, apparent in the pressure-dependence of T_{IM} , is a new and unexpected finding, unpredicted by the simple linear extrapolation of the low-pressure data available in literature. The present data are successfully described by the empirical curve

$$T_{IM}(P) = T_{\infty} - [T_{\infty} - T_{IM}(0)]exp(-P/P^*) \quad (1)$$

with $T_{\infty}=299\pm 3$ K and $P^*=3.4 \pm 0.4$ GPa. Using structural data at high pressure [27], we estimated the pressure dependence of W_0 [8] and, hence, the bare structural contribution to $T_{IM}(P)$ (dashed line in Fig. 3a). It is apparent that the bare contribution alone does not account for the observed rapid rise of T_{IM} at low-pressure, but a considerable pressure-driven weakening of the EPC, that is a considerable broadening of the effective bandwidth W_{eff} (i.e. $\xi \rightarrow 1$), is necessary. On the contrary, the bare structural term adequately reproduces the low P-sensitivity in the high-pressure regime. These findings are also supported by the simple argument offered by the Clausius-Clapeyron equation, that is $dT_{IM}/dP = \Delta v/\Delta s$. The rapid decrease of dT_{IM}/dP vs P should be more likely attributed to a reduction of the volume variation Δv than to an increase of the entropy variation Δs . Indeed, applied pressure is expected to diminish the octahedral distortion in the insulating phase, thus reducing the volume discontinuity Δv at the IM transition. The remarkable decrease of volume effects, recently reported for $R_A > 1.22$ Å [19], is also consistent with the vanishingly small values of dT_{IM}/dP at high pressure (i.e. $\Delta v \rightarrow 0$)

To state Eq. 1 in terms of a general law, we applied it to extract the dependence of T_{IM} on R_A at ambient pressure starting from a compound with a given R_A^0 . No adjustable parameter was introduced and only the *internal*/external pressure conversion was exploited through the variable substitution $P = (R_A - R_A^0)/\beta$. The $T_{IM}(R_A)$ curve thus obtained is shown in Fig. 3b in comparison with the experimental data of several compounds at constant $x=0.25$ doping (Ref. 20). The agreement is excellent up to $R_A \sim 1.22$ Å, that is over the region corresponding to IC regime, and first order IM transition [19, 20]. At larger R_A values (continuous transition [19, 20], WC regime) the curve fails to describe the experimental data. The

pressure derivative of Eq.1

$$\left. \frac{dT_{IM}(P)}{dP} \right|_P = \frac{T_\infty - T_{IM}(P)}{P^*} \quad (2)$$

is plotted versus $T_{IM}(P)$ in Fig. 4. Also shown in Fig. 4 are the zero-pressure limits of the experimental derivative $dT_{IM}(P)/dP|_{P=0}$ obtained from the present data (23 K/GPa) and from the $T_{IM}(P)$ data available in literature for other manganites [8, 9, 10, 11, 12, 13, 14, 15, 16, 17]. Also in this case, Eq. 2 describes the IC regime rather well, at least for $T_{IM} > 200$ K, whereas it is not appropriate for WC compounds (blue symbols). The deviation of the low T_{IM} (≤ 200 K) compounds from Eq.2 can be explained by the EPC getting stronger, with the localizing effect being strengthened by a high cation disorder [22, 30]. More quantitatively, for these samples the mean square deviation σ_{cat} of the $A-A'$ ion radii is larger than the mean square thermal displacement σ_{th} , obtained from the experimental vibrational frequencies of the $A-A'$ ions. This results in an *effective disorder* $\Sigma_{eff} = \sigma_{cat}/\sigma_{th} > 1$. The universal behaviour here observed (Fig. 4) shows that, regardless of doping or chemical composition, T_{IM} (i.e. W_{eff}) is actually the only relevant parameter for IC manganites. ($\Sigma_{eff} < 1$).

The present study offers the opportunity of separating the contributions of the bare structural effects from the pressure-tuned EPC. The latter plays an essential role up to $P \approx 2P^*$ (≈ 7 GPa), beyond which pressure-driven structural effects are sufficient to describe the IM transition curve (Fig. 3a). When reverted into an R_A -dependence, the pressure-dependence of T_{IM} , which shadows the EPC pressure-dependence, emphasises the full applicability of the model to IC systems (Fig. 3b). The departure of WC systems from the model curve suggests an abrupt readjustment of the balance among the different interactions. Indeed, when the internal/external pressure exceed a certain value (i.e. $R_A \rightarrow 1.22 \text{ \AA}$ or $P > 2P^*$) their effect is no longer equivalent: while P leaves unchanged both the crystal symmetry and the EPC strength, R_A induces a structural transition from orthorhombic to rhombohedral, whose higher symmetry does not allow for the static JT distortion [19]. The transition from the IC to the WC regime is not continuous and cannot be achieved by simply tuning the EPC by means of external pressure. Eq. 1 enables to clearly distinguish between the two regimes and represents a strict benchmark for any theoretical model aimed at addressing the complex physics of these systems.

Figure Captions.

Fig. 1 T -dependent optical densities measured along three representative isobars. On cooling down, the overall absorption at first decreases (red curves, insulator) and then increases (blue curves, metal) as shown by the broken arrows. Data over 1850-2450 cm^{-1} frequency range are not shown since the strong absorption from the diamonds affects the data quality.

Fig. 2 Temperature dependence of the spectral weight n^* along seven isobaric paths. Red and blue symbols refer to insulating and metallic behaviour respectively, lines are a guide to the eye.

Fig. 3 a) $P - T$ phase diagram of $\text{La}_{0.75}\text{Ca}_{0.25}\text{MnO}_3$. The grey line is the best-fit curve from Eq. 1 ($T_\infty=299$ K and $P^*=3.4$ GPa) to the present experimental data (half-filled circles).

b) $R_A - T$ phase diagram for $x=0.25$ manganites: diamonds from Ref. 20, the grey line is obtained from Eq. 1 exploiting the internal-external pressure conversion with no adjustable parameters $T_{IM}(R_A) = T_\infty - [T_\infty - T_{IM}(R_A^0)] \exp[-(R_A - R_A^0)/(\beta/P^*)]$. To make the data internally comparable, the R_A values of Ref. 20 have been recalculated using the ionic radii with coordination number 9 (Ref. 5) instead of 12 (ref. 20). The corresponding pressure scale is shown on the top x-axis.

Fig. 4 T_{IM} pressure derivative vs. T_{IM} . Zero pressure limit ($dT_{IM}(P)/dP|_{P=0}$ vs. $T_{IM}(0)$): bold half-filled circle, present experiment; diamonds data from literature (the reference number is also shown). Light half-filled circles show $dT_{IM}(P)/dP|_P$ vs. $T_{IM}(P)$ from the present experiment. The grey line is from Eq. 2.

References

- [1] Jin, S. *et al.* Thousandfold change in resistivity in magneto resistive La-Ca-Mn-O films. *Science* **264**, 413 (1994).
- [2] Millis, A. J. Lattice effects in magnetoresistive manganese perovskites *Nature* **392**, 147 (1998).
- [3] Millis, A. J. *et al.* Double exchange alone does not explain the resistivity of $\text{La}_{1-x}\text{Sr}_x\text{MnO}_3$. *Phys. Rev. Lett.* **74**, 5144 (1995).
- [4] Congeduti, A. *et al.* Infrared study of charge delocalization induced by pressure in the $\text{La}_{0.75}\text{Ca}_{0.25}\text{MnO}_3$ manganite. *Phys. Rev. B* **63**, 184410 (2001).
- [5] Hwang, H.Y. *et al.* Lattice effects on the magnetoresistance in doped LaMnO_3 . *Phys. Rev. Lett.* **75**, 914 (1995).

- [6] Guo-meng, Zhao *et al.* Giant oxygen isotope shift in the magnetoresistive perovskite $\text{La}_{1-x}\text{Ca}_x\text{MnO}_{3+y}$. *Nature* **381**, 676 (1996).
- [7] Cheong, S.W. and Hwang, H.Y. in *Colossal Magnetoresistance Oxides* edited by Tokura, Y. Gordon and Breach New York 2000.
- [8] Laukhin, V. *et al.* Pressure effects on the metal-insulator transition in magnetoresistive manganese perovskites. *Phys. Rev. B* **56**, R10009 (1997).
- [9] Hwang, H.Y. *et al.* Pressure effects on the magnetoresistance in doped manganese perovskites. *Phys. Rev. B* **52**, 15046 (1995).
- [10] Neumeier, J.J. *et al.* Substantial pressure effects on the electrical resistivity and ferromagnetic transition temperature of $\text{La}_{1-x}\text{Ca}_x\text{MnO}_3$. *Phys. Rev. B* **52**, R7006 (1995).
- [11] De Teresa, J.M. *et al.* Spontaneous behavior and magnetic field and pressure effects on $\text{La}_{2/3}\text{Ca}_{1/3}\text{MnO}_3$ perovskite. *Phys. Rev. B* **54**, 1187 (1996).
- [12] Wang, Y.S. *et al.* Oxygen-isotope effects on $\text{La}_{0.65}\text{Ca}_{0.35}\text{MnO}_3$ under pressure. *Phys. Rev. B* **60**, R14998 (1999).
- [13] Moritomo, Y. *et al.* Chemical and external pressure effects on ferromagnetic manganites. *Physica B* **237-8**, 26 (1997).
- [14] Arnold, Z. *et al.* Pressure effect on yttrium doped $\text{La}_{0.60}\text{Y}_{0.07}\text{Ca}_{0.33}\text{MnO}_3$ compound. *Appl. Phys. Lett.* **67**, 2875 (1995).
- [15] Khazeni, K. *et al.* Effect of Pressure on the Magnetoresistance of Single Crystal $\text{Nd}_{0.5}\text{Sr}_{0.36}\text{Pb}_{0.14}\text{MnO}_3$. *Phys. Rev. Lett.* **76**, 295 (1996).
- [16] Khazeni, K. *et al.* Pressure dependence of the resistivity and magnetoresistance in single-crystal $\text{Nd}_{0.62}\text{Pb}_{0.30}\text{MnO}_3$. *J. Phys. Cond. Matt.* **8**, 7723 (1996).
- [17] Kuwahara, H. *et al.* Spin-charge-lattice coupled phase transitions in bandwidth-controlled systems: $(\text{Nd,Sm})_{1/2}\text{Sr}_{1/2}\text{MnO}_3$. *Phys. Rev. B* **56**, 9386 (1997).
- [18] Millis, A.J. *et al.* Fermi-liquid-to-polaron crossover. II Double exchange and the physics of Colossal Magnetoresistance. *Phys. Rev. B* **54**, 5405 (1996).

- [19] Mira, J. *et al.* Strong reduction of lattice effects in mixed-valence manganites related to crystal symmetry. *Phys. Rev. B* **65**, 024418 (2001).
- [20] Fujishiro, H. *et al.* First-order-like ferromagnetic transition in $(\text{La}_{1-y}\text{Pr}_y)_{1-x}(\text{Ca}_{1-z}\text{Sr}_z)_x \text{MnO}_3$ ($x=0.25$). *Physica B* **281&282**, 491 (2000).
- [21] Röder, H. *et al.* Lattice Effects in the Colossal-Magnetoresistance Manganites. *Phys. Rev. Lett.* **76**, 1356 (1996).
- [22] Fontcuberta, J. *et al.* Local disorder effects on the pressure dependence of the metal-insulator transition in manganese perovskite *Appl. Phys. Lett.* **72**, 2607 (1998).
- [23] Kim, K. H. *et al.* Polaron Absorption in a Perovskite Manganite $\text{La}_{0.7}\text{Ca}_{0.3}\text{MnO}_3$. *Phys. Rev. Lett.* **81**, 1517 (1998).
- [24] Quijada, M. *et al.* Optical conductivity of manganites: Crossover from Jahn-Teller small polaron to coherent transport in the ferromagnetic state. *Phys. Rev. B* **58**, 16093 (1998).
- [25] Chattopadhyay, A. *et al.* Optical spectral weights and the ferromagnetic transition temperature of colossal magneto resistance manganites: Relevance of double exchange to real materials. *Phys. Rev. B* **61**, 10738 (2000).
- [26] Citroni, M. *et al.* Laser-Induced selectivity for dimerization versus polymerization of butadiene under pressure. *Science* **295**, 2058 (2002).
- [27] Meneghini, C. *et al.* High-pressure structure and electronic transport in hole-doped $\text{La}_{3/4}\text{Ca}_{1/4}\text{MnO}_3$ perovskites. *Phys. Rev. B* **65**, 012111 (2002).
- [28] Calvani, P. Optical properties of polarons. *Nuovo Cimento* **24**, num. 8 (2001) and references therein.
- [29] Congeduti, A. *et al.* Anomalous high-pressure dependence of the Jahn-Teller phonon in $\text{La}_{0.75}\text{Ca}_{0.25}\text{MnO}_3$. *Phys. Rev. Lett.* **86**, 1251 (2001).
- [30] Roudriguez-Martinez, L. M. *et al.* Cation disorder and size effects in magnetoresistive manganese oxide perovskites. *Phys. Rev. B* **54**, R15622 (1997).

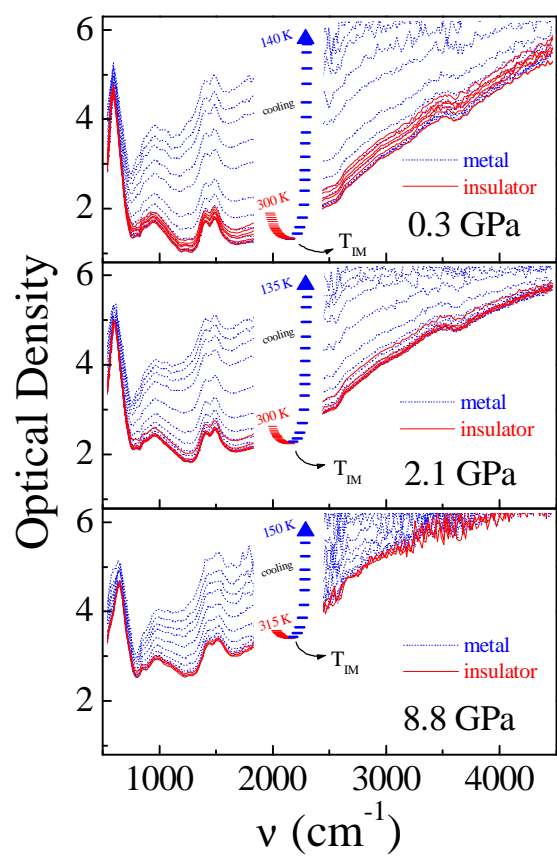


Figure 1

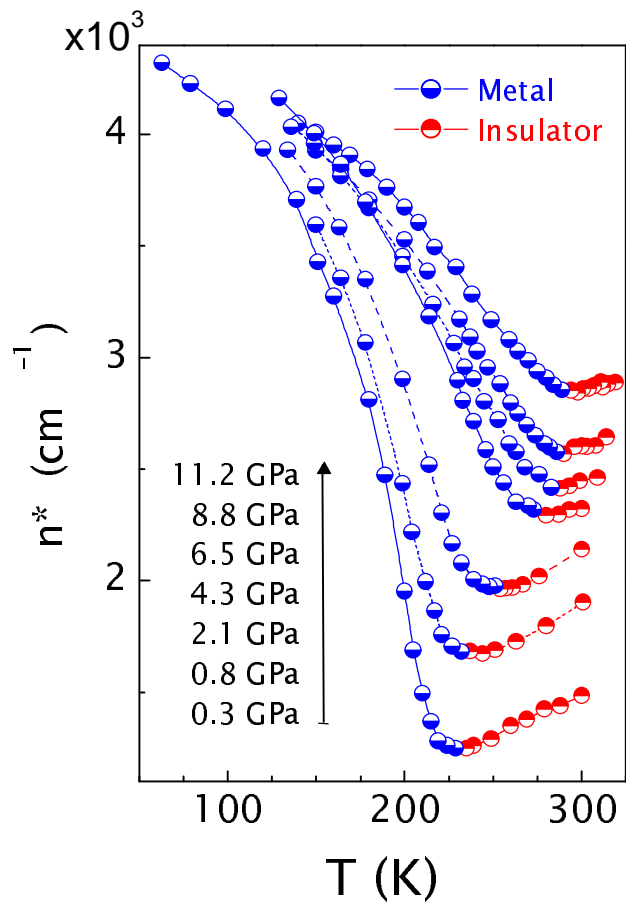


Figure 2

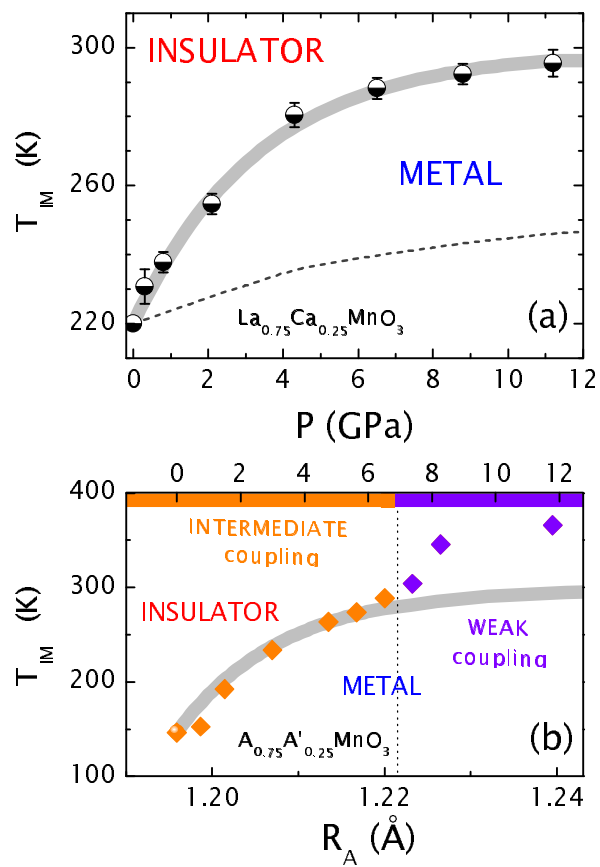


Figure 3

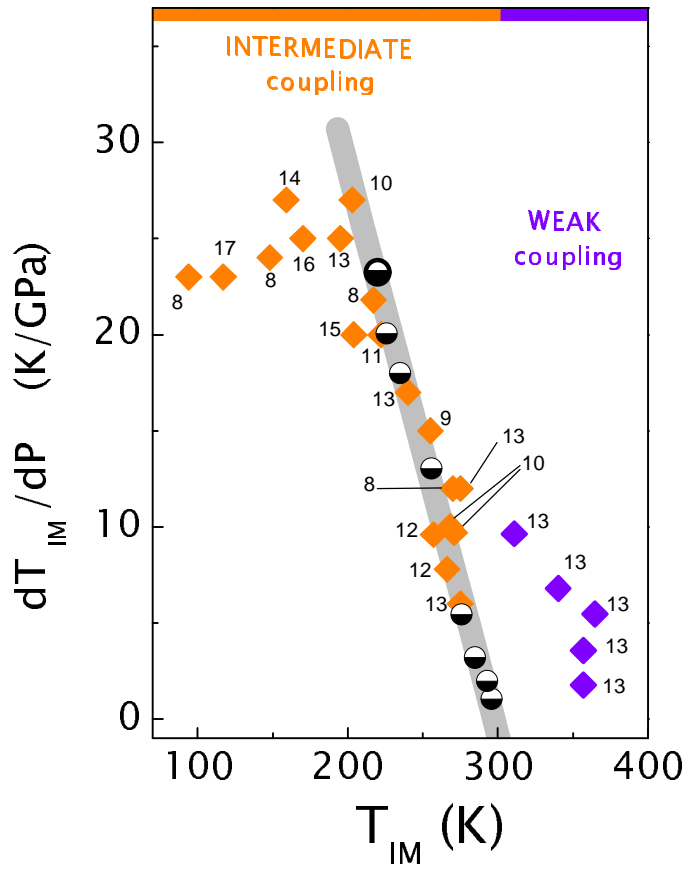


Figure 4